Int.J.Hydrogen Energy Vol. 43 (7), pp. 3822-3836, 2018
doi.org/10.1016/j.ijhydene.2017.12.166

Premixed hydrogen-air flames interacting with a hydrogen porous wall

Prashant S. Salimath[a], Ivar S. Ertesvåg[a,*], Andrea Gruber[b]

[a]*Department of Energy and Process Engineering, NTNU Norwegian University of Science and Technology, Kolbjørn Hejes vei 1b, NO-7491 Trondheim, Norway*
[b]*SINTEF Energy Research, Trondheim, Norway*

Abstract

A laminar one-dimensional hydrogen-air flame travelling and quenching towards a chemically inert permeable wall (PW) is studied. Hydrogen flows through the wall into the premixed H_2-air. The S3D numerical code with detailed chemistry is used. PW results are compared against results of an impermeable wall (IW), including effects of varying wall mass flux, stoichiometry, inert dilution and unburned-gas and wall temperatures. The maximum reaction heat release rate occurs at the wall in all cases. For rich and stoichiometric mixtures, PW with fuel influx gave a moderate reduction of the quenching (i.e. maximum) wall heat flux compared to IW, whereas for a lean mixture, the increase is considerable. Effects of the fuel influx on the importance of individual elementary reactions and radicals and intermediate species are investigated. The lean PW cases have similarities to much richer IW cases. Both a lower wall temperature and dilution reduce the burned-mixture temperature and, consequently, the wall heat flux.

Keywords: Permeable wall; S3D; Head on quenching; Flame-wall interaction; Wall heat flux; Detailed chemical mechanism

*Corresponding author. Phone: +47 73593839, Fax: +47 73593580
Email addresses: Prashant.Salimath@ntnu.no (Prashant S. Salimath), Ivar.S.Ertesvag@ntnu.no (Ivar S. Ertesvåg), Andrea.Gruber@sintef.no (Andrea Gruber)

1. Introduction

Thermal degradation of hardware parts that are subjected to large wall heat fluxes during flame-wall interactions (FWI) is a critical issue in many energy conversion devices, such as internal combustion engines, gas turbine combustors and furnaces. The premixed FWI can be described as coupled thermo-chemical processes involving high temperature, propagating premixed flames impinging on colder walls, where flame quenching occurs at a normal distance from the wall known as quenching distance [1, 2, 3, 4, 5, 6, 7, 8, 9]. Dreizler and Böhm [10] reviewed numerical and experimental FWI studies. They discussed the role of laser diagnostics development and validation of collected data through numerical simulations.

Flame quenching occurs with a large heat release near the wall, and the resulting wall heat flux reaches its maximum value. Accurate determination of the quenching distance and the corresponding wall heat flux is significant, as strong thermal gradients occur near the wall, affecting hardware durability, pollutants formation and engine performance. The different stages of FWI mechanisms are understood through high-fidelity numerics in simple laminar premixed flame configurations in one-dimensional (1-D) head-on quenching and 2-D side-wall quenching configurations.

Studies of transient quenching processes of flames have employed single-step and multi-steps chemical mechanisms. For low wall temperatures (around 300 K), the wall heat fluxes predicted by single-step chemical mechanisms have been seen to compare reasonably well to experimental observations. However, for higher wall temperatures these simple mechanisms have appeared to fail [11, 12, 4]. At high wall temperatures (above 400 K), it has been shown [6] that chemical processes play a significant role near the wall, involving exothermic radical recombination reactions. The detailed multi-step mechanisms employed in numerical codes have predicted well for wall heat fluxes and provided better understanding of radical recombination reactions involving radicals near the wall. Gruber et al. [3] showed that the role of exothermic radical recombination reactions was significant and contributed to 70% of the overall heat release at the wall for a laminar premixed

hydrogen-air flame. Dabireau et al. [5] demonstrated that in a premixed H_2–O_2 flame, the recombination reactions and reactions of intermediate species (HO_2, H_2O_2) together contributed 30% of the predicted wall heat flux.

Experimental study of FWI processes with quenching distances less than 1 mm near a wall is difficult due to strong thermal gradients [12, 13]. Therefore, we tend to rely on numerical simulations. FWI processes of impermeable wall configurations are described by a normalized wall heat flux and the quenching Peclet number, defined as the position of maximum fuel consumption rate and normalized by the flame thickness. For hydrocarbon fuels, it has been observed that the wall heat flux is inversely proportional to the flame quenching distance with an assumption that no thermal boundary layer exists between the wall and the near-wall unburnt mixture [14, 9, 12, 15]. Studies of hydrogen flames showed that their FWI behaviour differs from that of hydrocarbon flames for wall temperature maintained at 750 K, when quenching of the flame occurred much closer to the wall [5, 16, 7]. Owston et al. [7] extended the physical problem of [5] to a range between 298 and 1200 K and concluded that radical recombination reactions play a significant role in the evaluation of wall heat flux at higher wall temperatures.

The paper by Gruber et al. [17] (with two of the present authors) appears to be the first on numerical investigations on a fuel flux through a permeable wall into a flame. This potentially new design approach for combustion devices as a porous fuel diffuser possibly coated with H_2 selective permeable wall can replace conventional fuel nozzles and provide in-situ CO_2 - separation from the hydrogen fuel that is injected on the permeate side for mixing with the oxidant and combustion further downstream [18]. The hydrogen gas wall-permeation rate can influence the wall heat flux and avoid a flame coming very close to the wall. Hence, thermal degradation of hardware parts can potentially be reduced in comparison to an impermeable wall. Gruber et al. [17] discussed the transient nature of laminar FWI processes in 1-D and 2-D configurations and indicated a strong feedback mechanism between the permeating hydrogen flux and the flame on the permeate side.

A planar flame front propagates through a premixed fuel/air mixture towards a solid wall facing the flame. When reaching the wall, the flame

quenches. The process can be analyzed as a 1-dimensional case, and is illustrated schematically in Fig. 1 for an impermeable wall (IW) and a fuel-permeable wall (PW) configuration. Both walls have chemical inert properties, that is, no adsorption or catalytic effects. In the PW case, the flame is partly premixed, as pure fuel (here H_2) flows into the domain and mixes with premixed fuel-air mixture on the permeate side.

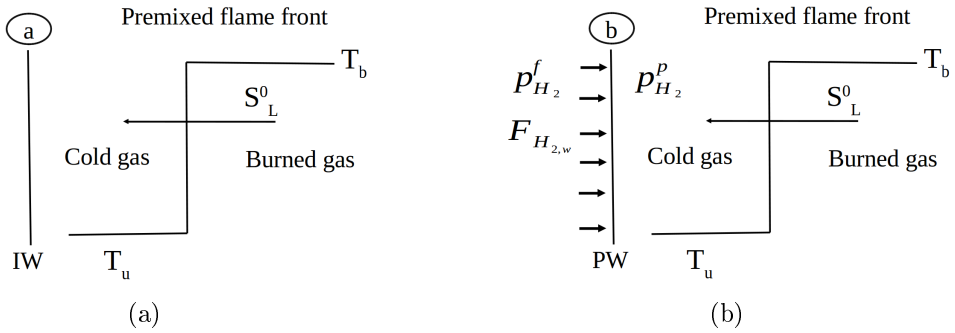

Fig. 1: Head-on quenching configurations of (a) Impermeable wall (IW) and (b) Permeable wall (PW) with hydrogen flux in accordance with Eq. 5

Some aspects of the problem were considered by Gruber et al. [17] as part of a larger study. Numerical simulations with a detailed chemical mechanism and diffusion mechanisms were conducted for laminar hydrogen-air flames at atmospheric pressure on a planar and permeable (hydrogen selective) wall at constant wall temperature of 750 K and different H_2/air mixtures. It was found that for IW, the wall heat flux ($-\Phi_w$) was slightly reduced and the quenching delayed in time as the undisturbed-mixture equivalence ratio (ϕ_u) was increased from 0.5 (fuel lean) to 1.5 (fuel rich). The net reaction heat release had its maximum point at the wall and it was larger for a stoichiometric mixture than for rich or lean mixtures. The temperature of the reacted mixture close to the wall around quenching approached, but was less than, the burned temperature of the freely propagating flame. The local equivalence ratio decreased towards the burned-mixture value as the flame front reached the wall and quenched. The PW cases of [17] were all conducted with a single permeate feed pressure (10 bar).

In the present paper, the physical problem is extended to operate the porous fuel diffuser configuration with different feed pressures at the porous wall. The resulting variation in hydrogen flow through the membrane influences the local chemistry near the wall and the heat transfer. We will also investigate FWI characteristics of the PW configuration, influence of hydrogen mass flux on heat release rates near the wall and of varying feed pressure and equivalence ratio. Contributions of the individual elementary reactions will be studied more in detail. Furthermore, effects of dilution with N_2 (inert) and H_2O (participating) will be studied.

These studies can aid in better understanding of flame chemistry near the permeable wall. They can also provide novel concepts for hardware components referred to as impermeable walls with some degree of permeability of fuel such that large wall thermal fluxes are avoided. Some permeation of fuel through a basically impermeable wall can alter the local chemistry for a given stoichiometry during operation.

The following section will describe the choice of models and the numerical setup, including hydrogen flow across the wall through a membrane, numerical methods used for DNS studies, computational setup for performing 1-D transient runs, permeable wall boundary condition formulation and definitions related to FWI as well as some of the basic characteristics of the laminar, undisturbed flame in so far as it is important for the understanding of the flame-wall interaction results in the present paper. Sections 3 and 4 show results and following discussion. Finally, conclusions are presented.

2. Numerical setup and choice of models

2.1. Governing equations

The following equations represent governing reacting flows and are written in conservative form as [19]

$$\frac{\partial \rho}{\partial t} = \frac{\partial}{\partial x_\alpha}(-\rho u_\alpha), \tag{1}$$

$$\frac{\partial}{\partial t}(\rho u_\alpha) = \frac{\partial}{\partial x_\beta}\left(-\rho u_\alpha \cdot u_\beta\right) + \frac{\partial}{\partial x_\beta}(\tau_{\beta\alpha}) - \frac{\partial p}{\partial x_\alpha}, \tag{2}$$

$$\frac{\partial}{\partial t}(\rho e_0) = \frac{\partial}{\partial x_\beta}\left[-\left(\rho e_0 + p\right) u_\beta\right] + \frac{\partial}{\partial x_\beta}\left(\tau_{\beta\alpha} \cdot u_\alpha\right) - \frac{\partial \Phi_\beta}{\partial x_\beta}, \tag{3}$$

$$\frac{\partial\left(\rho Y_k\right)}{\partial t} = \frac{\partial}{\partial x_\beta}\left(-\rho Y_k u_\beta\right) + \frac{\partial}{\partial x_\beta}\left(-\rho Y_k V_{\beta k}\right) + \dot{\omega}_k. \tag{4}$$

2.2. Mass flux through permeable wall

The hydrogen permeation through permeable wall (also referred as membrane wall) is based on Sieverts' law of hydrogen diffusion in thin Pd-Ag based membranes. The hydrogen flux formulation is based on palladium or palladium alloy membranes that proceeds via a solution-diffusion mechanism and generally expressed for species H_2 as [20, 21, 17]

$$F_{\mathrm{H_2,w}} = Q^{''} \cdot W_{\mathrm{H_2}} \left((p^{\mathrm{f}}_{\mathrm{H_2}})^n - (p^{p}_{\mathrm{H_2}})^n \right), \tag{5}$$

where $Q^{''}$ and n are the membrane permanence factor and the pressure exponent, respectively, of Pd-based membranes. For typical 2-3 μm Pd-based membrane thickness, these values were set to $Q^{''} = 7.0 \cdot 10^{-6}\,\mathrm{kmol/(m^2 s Pa^{0.5})}$ and $n = 0.5$ [20, 17] .

2.3. Chemical mechanism

The hydrogen-oxygen chemistry was described by the mechanism of Li et al. [22], with 8 species (H_2, O_2, H_2O, OH, H, O, HO_2 and H_2O_2) and 19 steps, supplemented with N_2 as an inert gas. This approach enabled identifying the most important species, radicals and reaction rates during the flame quenching process. Table 1 lists the 19 two-way elementary reactions, which will be denoted as R1 to R19 with the enumeration in accordance with [22] (also in [17]) and f and r denoting forward and reverse reactions.

2.4. Numerical method

The 3-D code S3D, developed at Sandia National Laboratories, was modified for the one-dimensional configuration to perform FWI simulations. The

Table 1: Elementary reactions in the H_2–O_2 chemical mechanism, Li et al. [22].

No.	Reactions
R1	$O_2 + H \rightleftharpoons OH + O$
R2	$H_2 + O \rightleftharpoons OH + H$
R3	$OH + H_2 \rightleftharpoons H + H_2O$
R4	$H_2O + O \rightleftharpoons 2OH$
R5	$H_2 + M \rightleftharpoons 2H + M$
R6	$2O + M \rightleftharpoons O_2 + M$
R7	$H + O + M \rightleftharpoons OH + M$
R8	$OH + H + M \rightleftharpoons H_2O + M$
R9	$O_2 + H + M \rightleftharpoons HO_2 + M$
R10	$H + HO_2 \rightleftharpoons O_2 + H_2$
R11	$H + HO_2 \rightleftharpoons 2OH$
R12	$O + HO_2 \rightleftharpoons OH + O_2$
R13	$OH + HO_2 \rightleftharpoons O_2 + H_2O$
R14	$2HO_2 \rightleftharpoons O_2 + H_2O_2$
R15	$H_2O_2 + M \rightleftharpoons 2OH + M$
R16	$H + H_2O_2 \rightleftharpoons OH + H_2O$
R17	$H + H_2O_2 \rightleftharpoons H_2 + HO_2$
R18	$O + H_2O_2 \rightleftharpoons HO_2 + OH$
R19	$OH + H_2O_2 \rightleftharpoons H_2O + HO_2$

compressible Navier-Stokes equations were solved in conservative form on a structured mesh. The code used the Message Passing Interface (MPI) for inter-process communication in parallel execution [23] and can easily be ported in different architectures [24] for different high end performance studies [24, 3, 25, 26, 27, 28, 29].

The solver had a non-dissipative numerical scheme with an eight-order explicit central differential scheme in space (third order, one-sided stencils at the domain boundaries) and a fourth-order explicit Runge-Kutta method in time [30]. High-frequency spurious fluctuations and aliasing errors in solutions were removed using a tenth-order purely dissipative spatial filter.

The constitutive relationships, such as ideal gas equation of state, models for reaction rates, molecular transport and thermodynamic properties details, were described in [19]. The code could handle multi-step chemistry. The

thermodynamic properties and mixture-averaged transport properties were evaluated through linking of Chemkin and Transport software libraries [31, 32] to the S3D solver.

2.5. Boundary conditions

The permeable wall boundary formulation was based on no-slip, isothermal and species zero-gradient conditions, except for H_2. The hydrogen mass fraction gradient at the wall was set by the expression for permeability, $F_{H_2,w}$ (Eq. (5)). The well-posed solution [33, 34, 35] for the permeable wall can be expressed as

$$u_\alpha = 0, \tag{6}$$

$$T_w = T_u, \tag{7}$$

$$\left(\frac{\partial Y_{H_2}}{\partial x_\alpha}\right)_w = \frac{F_{H_2,w}}{\rho_w D_{mix,w}} \tag{8}$$

and

$$\left(\frac{\partial Y_k}{\partial x_\alpha}\right)_w = 0 \text{ for } k \neq H_2. \tag{9}$$

In the wall-normal direction, the non-zero velocity component was estimated as $u_1 = F_{H_2,w}/\rho_{H_2}$. The wall pressure gradient was expressed by inserting the species mass fluxes $F_k = \rho_k u_\alpha$ into the momentum equation (Eq. 2), with the assumption of wall-normal gradients of these fluxes set to zero. The pressure gradient at the wall was then obtained as

$$\left(\frac{\partial P}{\partial x_\beta}\right)_w = -\left(\sum_{k=1}^{N_g} \frac{\partial F_{k,w}}{\partial t}\right) - \left(\frac{\partial u_\beta}{\partial x_\beta} \cdot \sum_{k=1}^{N_g} F_k\right)_w + \left(\frac{\partial \tau_{\alpha\beta}}{\partial x_\beta}\right)_w. \tag{10}$$

Here, only hydrogen contributed to the sum taken over all gases. The first and second terms on the right hand side of Eq. 10 represent the unsteady and steady terms as consequences to wall-normal momentum of the permeable wall due to hydrogen flux. At the wall, the mass fractions of species ($Y_{k,w}$) and the pressure (P_w) were extracted by inverting the numerical stencil. The density at the wall, ρ_w, could then be updated using these values and the wall temperature in the ideal-gas equation of state.

The impermeable wall boundary condition was similar to the above, with the simplification that no mass penetrated the wall. That is, Eq. 9 was used for H_2 as well, and the RHS of Eq. 10 was reduced to the viscous term.

For the outflow boundary at the right-hand side of the domain, the Navies-Stokes characteristic boundary conditions (NSCBC) [36, 37] were used for both IW and PW cases.

2.6. Definitions, non-dimensional quantities

The incident wall heat flux was calculated as $\Phi_\mathrm{w} = \lambda(\partial T/\partial x)_\mathrm{w}$. The maximum value that occurred at quenching was denoted as $\Phi_\mathrm{w,Q}$. The quenching instance was taken as the time when the wall heat flux had its maximum value [6]. During the quenching process, we tracked the flame position through the locations of the maximum reaction heat release rate (y_{ω_max}) and the maximum fuel consumption rate ($y_{\omega_\mathrm{F,max}}$) in the flame. The corresponding wall-to-flame distances were normalized by the characteristic flame thickness $\delta_\mathrm{L} = \lambda_\mathrm{u}/(\rho_\mathrm{u} C_{p,\mathrm{u}} S_\mathrm{L}^0)$ [5] to yield the respective Peclet numbers, $\mathrm{Pe} = y_{\omega_\mathrm{max}}/\delta_\mathrm{L}$ and $\mathrm{Pe_F} = y_{\omega_\mathrm{F,max}}/\delta_\mathrm{L}$.

The flame speed S_L^0, the flame thickness δ_L and the laminar flame power $q_l^0 = \rho_\mathrm{u} C_{p,\mathrm{u}} S_\mathrm{L}^0 (T_\mathrm{b} - T_\mathrm{u})$ were calculated for the flame propagating through the undisturbed gas mixture before reaching the wall. The burnt temperature T_b was evaluated as the equilibrium adiabatic flame temperature of this freely propagating flame. The thermal flame thickness was defined as $\delta_\mathrm{L}^0 = (T_\mathrm{b} - T_\mathrm{u})/(\partial T/\partial x)_\mathrm{max}$ [14] and the non-dimensional flame thickness as $\delta_\mathrm{L}^* = \delta_\mathrm{L}^0/\delta_\mathrm{L}$.

Non-dimensional variables were introduced, such as the heat release rate $\dot{\omega}^* = \dot{\omega}\delta_\mathrm{L}/q_l^0$ and fuel consumption rate $-\dot{\omega}_\mathrm{F}^* = \int_0^L (-\dot{\omega}_\mathrm{F}) dx/(\rho_\mathrm{u} S_\mathrm{L}^0 Y_\mathrm{F,u})$. The non-dimensional wall heat flux was given as $\Phi_\mathrm{w}^* = \Phi_\mathrm{w}/q_l^0$.

All time instants were normalized by the laminar flame timescale as $t^* = t \cdot S_\mathrm{L}^0/\delta_\mathrm{L}$. In the cases of PW, the normalized mass flux was defined as $F_{\mathrm{H_2,w}}^* = F_{\mathrm{H_2,w}}/F_{\mathrm{H_2max}}$, where $F_{\mathrm{H_2max}}$ was the maximum wall mass flux evaluated (Eq. 5) for a zero hydrogen partial pressure on the permeate side.

The timescale of flame-wall interaction for head-on quenching, t_FWI, was defined [13] as the time required for Φ_w to reach the maximum wall flux from one-half of this maximum. It was normalized as $t_\mathrm{FWI}^* = t_\mathrm{FWI} \cdot S_\mathrm{L}^0/\delta_\mathrm{L}$.

2.7. Specifications of the present investigations

The initial flow field of each H_2-air flame was placed in the center of the one-dimensional domain. The quiescent initial field solutions were computed based on Chemkin Premix [32]. A progress variable function was used in the initialization to map all points in the one-dimensional domain taken from Chemkin Premix.

The computational domain had a length of $L = 0.02\,\mathrm{m}$ and was characterized by a uniform mesh in the wall-normal direction. The number of nodes, $N = 4096$, was chosen from a grid sensitivity study for PW cases (see Sect. 3.1). The time step was fixed at $1.0{\cdot}10^{-9}\,\mathrm{s}$ for all simulations.

The species mass balance, Eq. (4), was solved for all species but N_2, which was determined from continuity of mass. The species reaction rates and all thermal properties were calculated at every step of the iteration.

The Soret effect (thermo-diffusion) and pressure diffusion were taken into account, whereas the Dufour effect was not implemented in S3D [19]. Radiation heat transfer and body-force effects (gravity) were neglected.

Air was assumed as a mixture of 79% N_2 and 21% O_2, molar based. The pressure of the gas mixture was maintained at 1 atm. The temperature of the unburned gas and the wall was specified at $T_\mathrm{u} = T_\mathrm{w} = 750\,\mathrm{K}$, except when the effects of this temperature was studied (then, 300 K and 500 K). The initial velocities were set to zero for all cases.

Four PW cases of constant $p^\mathrm{f}_{\mathrm{H}_2} = 10.0$, 5.0, 2.0 and 1.0 atm and the IW case were investigated for each of four fuel-air conditions, $\phi_\mathrm{u} = 0.5$, 0.8, 1.0 and 1.5. These equivalence ratios pertained to the undisturbed mixture, unaffected by the fuel influx from the wall. Accordingly, for PW the permeation commenced at $t = 0$. Due to lack of experimental results on PW configurations, the results were compared against the impermeable wall configuration for validation purposes. This can also give comparison to previous flame quenching results for hydrogen flames [5, 7].

In the previous study [17] was seen that for PW, the local equivalence ratio at the wall was in the range 3–5. Therefore, an IW case was run here with $\phi_\mathrm{u} = 4.0$ ($T_\mathrm{u} = T_\mathrm{w} = 750\,\mathrm{K}$) for comparison with the leaner PW. Furthermore, cases with dilution by N_2 and H_2O were investigated,

and also cases with lower unburnt-gas and wall temperature, as specified in Sections 3.4 and 3.5 below.

3. Results

3.1. Initial investigations for validation

In order to ensure quasi-steady conditions, the flame profile was initiated sufficiently far from the wall (i.e. $x = L/2$) before the flame propagated towards the wall. The initialization method described in Sect. 2.7 yielded marginally incorrect initial fields during flame set-up. Initial spurious oscillation was observed in the transient term at $t^* = 58.5$. This indicated discontinuities, however, which could be ignored as the behavior was short and far from the flame quenching time. The propagating flame readjusted within the unburnt mixture and reached a nearly constant flame speed until it sensed the presence of the wall or enriched hydrogen fuel concentration due to permeation. Therefore, the period before $t^* = 60$ was ignored in the analyses of the results.

The quenching times were quite similar for both cases, $t^*_{\mathrm{Q}} = 501.8$ for IW and $t^*_{\mathrm{Q}} = 503.97$ for PW. The actual values depend on the initial location of the flame and are not directly comparable to other studies. A difference was seen as for PW, the wall influence commenced much earlier, at approximately 0.80 times t^*_{Q} compared to 0.98 for IW. The first influence was weak, but an increased depletion (outflow) of mass was clearly seen in the results, although the permeation added mass to the system.

The total depletion of mass of the system for the time interval from $t^* = 60$ to 1640 was $1.48{\cdot}10^{-3}\,\mathrm{kg/m^2}$ (22% of the original mass) and $1.69{\cdot}10^{-3}\,\mathrm{kg/m^2}$ (25%), respectively, for IW and PW.

A sensitivity study was performed to find the sufficient resolution required to capture the wall thermal flux and the flame thickness during quenching. Table 2 presents this examination performed for PW cases at stoichiometric conditions with a varying number of grid points (N) for a feed pressure of $p^{\mathrm{f}}_{\mathrm{H_2}} = 10$ atm. It shows that for $N = 4096$, the quenching thermal flame thickness was then captured by a number of gridpoints, $M = 24$. Table 3

presents computations for varying ϕ_u at $N = 4096$. The results showed that this resolution captured the quenching flame thickness by 22-27 nodes for the PW cases and by 12-20 nodes for the IW cases. It was assumed that a resolution of 10 is sufficient [3]. Accordingly, $N = 4096$ was used for all cases.

3.2. Flame wall interaction (FWI) characteristics

Graphs showing the time evolution of wall-normal profiles of the normalized temperature, the normalized reaction heat release rate and the local equivalence ratio was shown by Gruber et al. [17] for undisturbed equivalence ratios ϕ_u of 0.5, 1.0 and 1.5, a wall temperature of 750 K and a feed pressure of $p^f_{H_2} = 10\,\text{bar}$. These graphs are not repeated here.

Figures 2 and 3 display FWI characteristics (δ^*_L, $-\dot{\omega}^*_F$, $\dot{\omega}^*$, Pe, Pe_F) plotted against non-dimensional time (t^*) for the case of $\phi_u = 1.0$, $T_u = T_w = 750\,\text{K}$, $p^f_{H_2} = 10\,\text{atm}$ and $N = 4096$. These figures present the premixed head-on-quenching process split into three stages [5]: Stage I is the undisturbed propagation. In Stage II, the wall influences the flame, while in Stage III, the overall reaction rate and wall heat flux decreases after quenching. Due to the hydrogen inflow, the ranges of these stages differs for PW compared to IW. In the undisturbed flow, the mass consumption rate and heat release rate were $-\dot{\omega}^*_F = 0.3015$ and $\dot{\omega}^* = 0.0414$. For IW, the former just declined towards zero after quenching, while the heat release rate came to a peak value

Table 2: Flame properties with varying grid points (N), obtained for PW cases at $\phi_u = 1.0$ and $p^f_{H_2} = 10$ atm.

N	δ^*_L	$\delta^*_{L,Q}$	$\Phi_{w,Q}$	M
[-]	[-]	[-]	[MW/m^2]	[-]
1024	26.60	8.56	2.752	9
2048	26.01	7.23	3.130	15
4096	25.90	5.87	3.295	24
8192	25.88	5.86	3.300	48

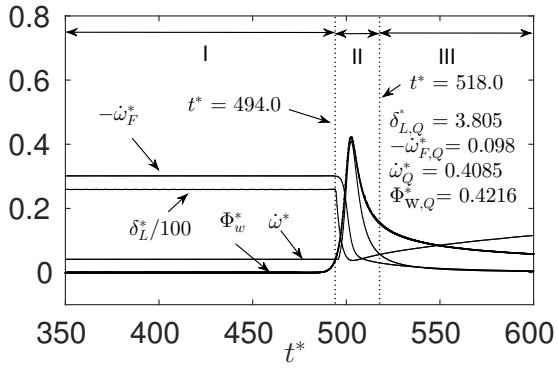

(a) IW case.

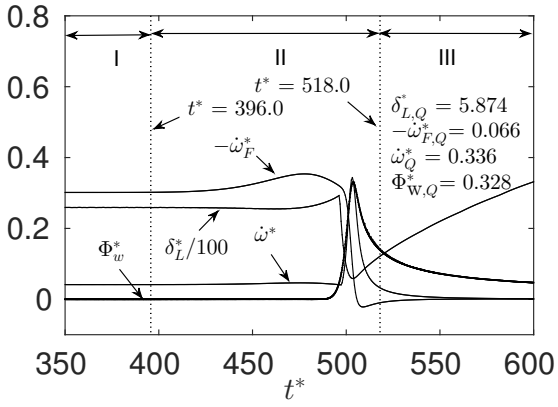

(b) PW case.

Fig. 2: Non-dimensional characteristic parameters versus non-dimensional time of premix FWI cases: Impermeable (top) and Permeable (bottom) wall boundaries. The unstretched laminar flame thickness and quenching values are included.

Table 3: Flame properties obtained for varying ϕ_{u} with given $N = 4096$ and $p^{\mathrm{f}}_{\mathrm{H_2}} = 10\,\mathrm{atm}$.

Wall type	ϕ_{u} [-]	S^0_{L} [m/s]	δ_{L} [10^{-6} m]	q^0_l [MW/m^2]	T_{b} [K]	δ^*_{L} [-]	$\delta^*_{\mathrm{L,Q}}$ [-]	$\Phi_{\mathrm{w,Q}}$ [MW/m^2]	M [-]
IW	0.5	6.40	26.11	4.12	2017.5	19.78	3.84	1.092	20
IW	1.0	10.8	19.73	10.05	2597.3	25.90	2.93	4.230	12
IW	1.5	12.5	19.88	11.22	2539.4	24.90	3.39	7.698	14
PW	0.5	6.40	26.11	4.12	2017.5	19.78	4.11	3.462	22
PW	1.0	10.8	19.73	10.05	2597.3	25.90	5.87	3.295	24
PW	1.5	12.5	19.88	11.22	2539.4	24.06	6.41	2.957	27

of $\dot{\omega}^* = 0.4085$ at $t^* = 503.0$ and then declined. For PW, both rates peaked: $-\dot{\omega}^*_{\mathrm{F}} = 0.3538$ at $t^* = 478.0$ and $\dot{\omega}^* = 0.3434$ at $t^* = 503.3$. The maximum heat release rate reached the wall (Pe = 0) at $t^* = 496.5$ for IW and at $t^* = 497.8$ for PW. The flame thickness came to a minimum of $\delta^*_{\mathrm{L}} = 3.775$ for IW at $t^* = 501.8$, that is, after quenching. For PW, it first had a minor increase and then fell to its minimum value just before quenching; $\delta^*_{\mathrm{L}} = 5.874$ at $t^* = 503.8$.

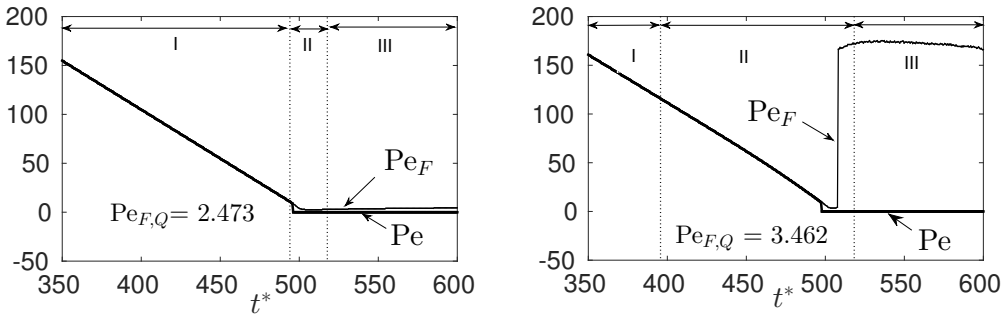

(a) IW case. (b) PW case.

Fig. 3: Peclet numbers versus non-dimensional time for Impermeable (a) and Permeable (b) wall configurations. The quenching values are included.

During the flame quenching process, the transient wall heat flux peaked due to a large overall heat release rate at the wall for both IW and PW. The heat release rates of the individual elementary reactions are shown in Fig. 4

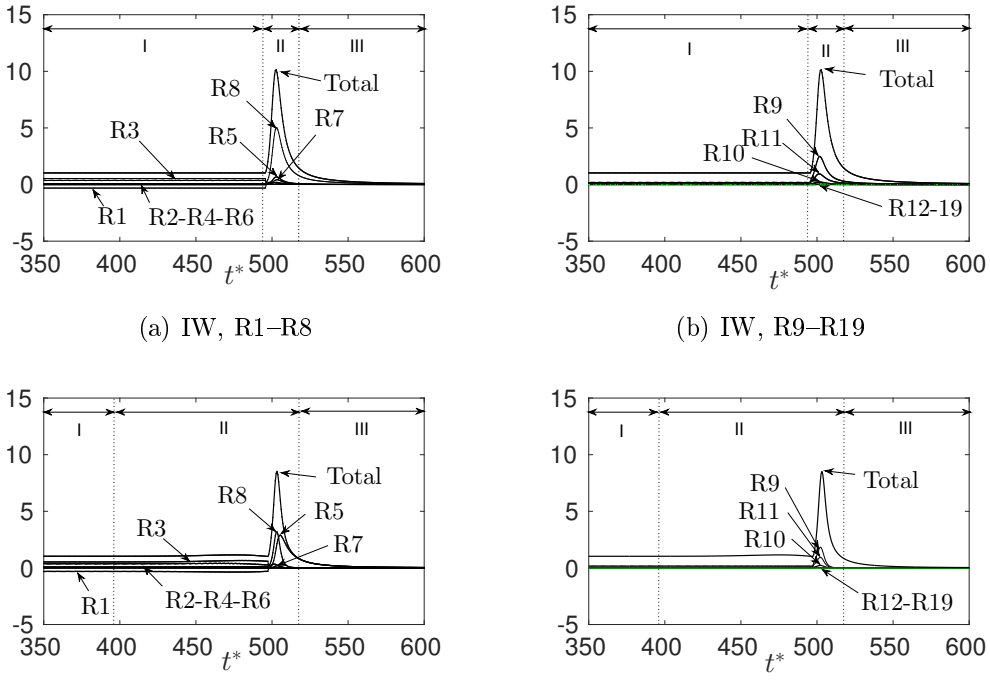

(a) IW, R1–R8

(b) IW, R9–R19

(c) PW, R1–R8

(d) PW, R9–R19

Fig. 4: Normalized heat release rates for overall (total) and elementary reactions are shown for IW and PW configurations. The overall heat release rate of the freely propagating flame is used for normalization.

and compared to the overall heat release. The heat release rates shown here and in Fig. 2 were calculated for the location of maximum net heat release rate. The cases of Figs. 4 and 5 were the same as in Figs. 2–3.

The transient wall H_2 mass flux of the PW configuration will be shown below. At stoichiometric conditions it spiked to a non-dimensional value of 0.81 at quenching from the value 0.79 just before.

Figure 5 displays transient mass fraction of all species (except N_2) at the wall (i.e. $x = 0$) for both IW and PW configurations.

3.3. Effects of varying feed pressure and equivalence ratio on PW configurations

In the following simulations the feed pressure ($p^{\mathrm{f}}_{\mathrm{H_2}}$) was varied, while the undisturbed gas mixture on the permeate side had stoichiometric conditions.

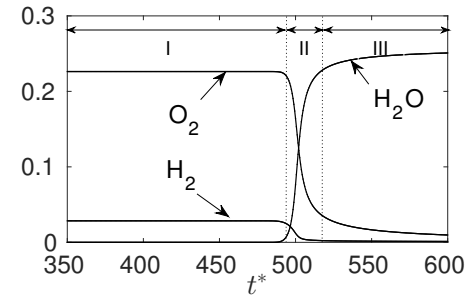

(a) Main species, IW

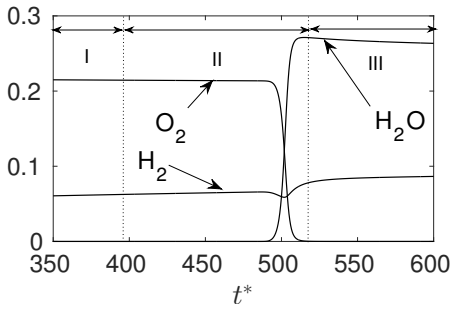

(b) Main species, PW

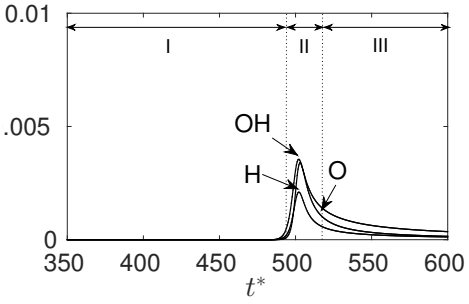

(c) Radical species, IW

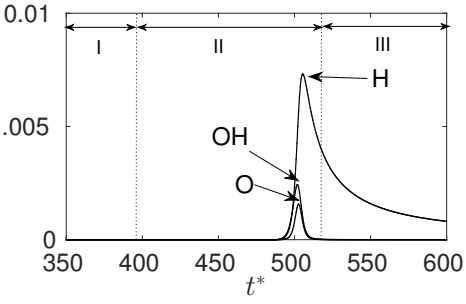

(d) Radical species, PW

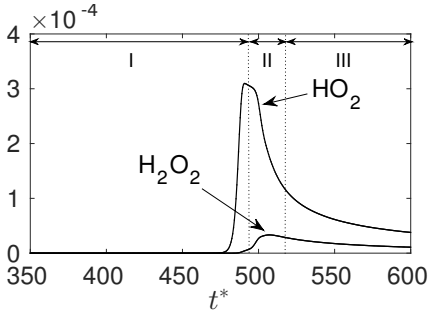

(e) Intermediate species, IW

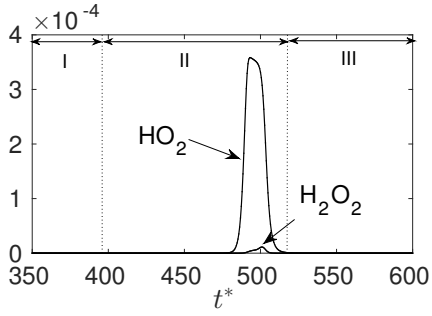

(f) Intermediate species, PW.

Fig. 5: Transient profiles of species mass fractions at the wall ($x = 0$), stoichiometric conditions.

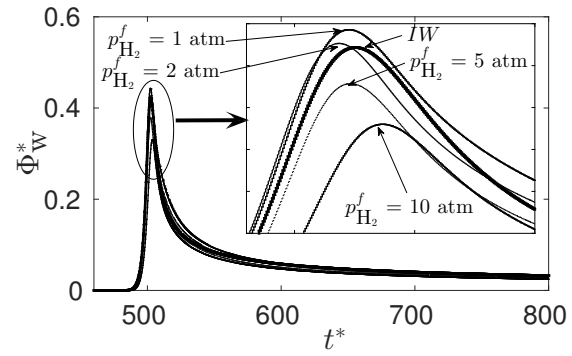

(a) Normalized wall heat fluxes, Φ^*_w.

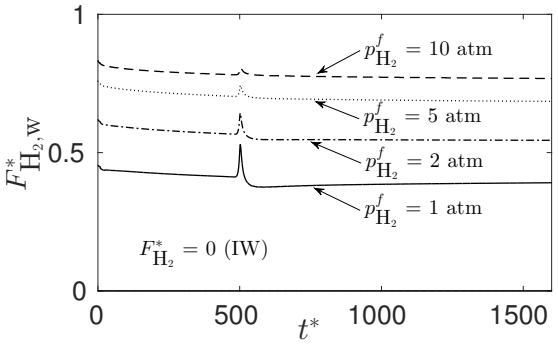

(b) Normalized wall mass fluxes, $F^*_{H_2,w}$.

Fig. 6: Transient wall heat fluxes (a) and mass fluxes (b) for different feed pressure ($p^f_{H_2}$) in FWI configurations at stoichiometric conditions. The IW configuration is also shown as a reference case for wall heat flux.

Figure 6 shows the transient wall heat fluxes and wall H_2 mass fluxes of four PW cases and the corresponding IW case at stoichiometric conditions. It was seen that increasing the feed pressure at the wall reduced the wall heat flux and delayed the quenching. Increasing feed pressure at the wall provided a higher hydrogen flux, influencing exothermic recombination reactions, mainly R8f, R9f and R11f, to reduce significantly the overall heat release rate. Increasing the H_2 wall flux promoted Reaction R5r such that exothermic recombination reactions at the wall were reduced in magnitude. The lower feed pressures ($p^f_{H_2}$ at 1.0 and 2.0 atm) gave quenching earlier than IW and at larger wall heat fluxes. The increased normalized hydrogen fluxes had lesser peaks at quenching for higher higher feed pressures.

For the rich and lean mixtures, FWI characteristics behaved qualitatively similar to the stoichiometric mixture described by Figs. 2–6. Among the few deviations were the wall heat transfer (reported in Fig. 3 of Gruber et al. [17]); that is, higher values with lower equivalence ratio for PW and vice versa for IW. Another observation here was that for the stoichiometric case (cf. Fig. 6a) and (more notable for) the rich case, increased feed pressure (increased wall influx) gave a delayed and reduced peak wall heat flux. For the lean case, the tendency was not as clear. Furthermore, for the rich flame $\mathrm{Pe_F}$ went to zero just before quenching and remained so for a while, whereas it for the stoichiometric and lean cases rose to a high value (cf. Fig. 3b). For the lean PW case, contrary to the stoichiometric case, $\mathrm{Pe_F}$ declined quite fast after the spike.

Figure 7 shows the normalized values for the wall H_2 mass flux, wall-to-flame distance (i.e., Peclet number) and the wall heat flux at quenching for varied feed pressure and equivalence ratio. The results obtained for the investigated cases are shown as points in the graphs. The lines between the points do not show more results but were supplemented to ease reading.

Since the local partial H_2 pressure just inside the wall ($p^{\mathrm{p}}_{\mathrm{H_2}}$) is directly related to $p^{\mathrm{f}}_{\mathrm{H_2}}$ and $F_{\mathrm{H_2,w}}$ through Eq. 5, Figs. 6b and 7a also indicate on that quantity.

It should be noted that the denominator of the dimensionless flux shown in Fig. 7a increases with the feed pressure, while it is independent of the equivalence ratio. This means that the absolute values increase more with feed pressure than those shown. The denominator of the Peclet number (laminar flame thickness) increases with increasing deviation from stoichiometry, while the denominator of the dimensionless heat flux (flame power) decreases. Both these denominators are independent of the feed pressure. Accordingly, the dimensional counterparts of Figs. 7b–c showed curves that were more assembled for PW. In particular, the lean cases were close to the stoichiometric cases. In other words, the dimensional wall heat flux at quenching (i.e. the maximum wall heat flux) was minorly affected by the initial equivalence ratio (ϕ_{u}) of the mixture. Increasing the feed pressure from 1 to 10 atm reduced the wall heat flux by about one-fourth, while the corresponding wall fuel

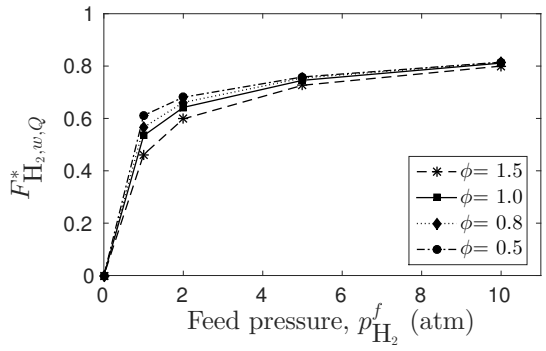

(a) Quenching wall H_2 mass flux, $F^*_{\mathrm{H_2,w,Q}}$.

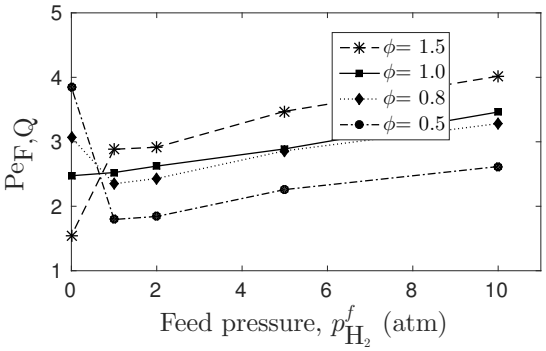

(b) Quenching Peclet number, $\mathrm{Pe_{F,Q}}$.

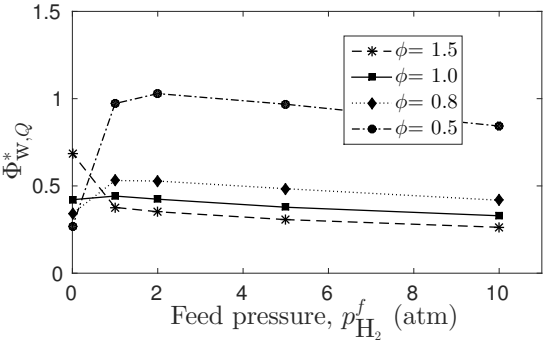

(c) Quenching wall heat flux, $\Phi^*_{\mathrm{w,Q}}$.

Fig. 7: Normalized quenching mass flux, wall-flame distance and wall heat flux for varying equivalence ratio and PW feed pressures. Zero feed pressure represents the IW case.

flux increased 4–5 times. In comparison, the rich ($\phi_u = 1.5$) IW case had a dimensional maximum wall heat flux about twice those of the stoichiometric IW case and all the PW cases, while the leaner IW case ($\phi_u = 0.5$) gave a value one-fourth of the stoichiometric.

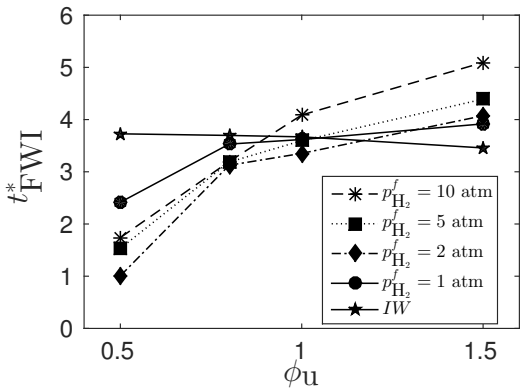

Fig. 8: Normalized time of flame-wall interaction for varying equivalence ratio of IW and PW at different feed pressures.

Non-dimensional FWI timescales are shown in Fig. 8 for IW and for PW at varying feed pressures. For PW they increased monotonically for increasing ϕ_u, while decreasing for IW. At rich conditions, the timescale increased with more permeation. For lean conditions, there was first a reduction to a feed pressure to 2 atm, and then an increase with further inrease of permeation.

Figure 9 displays the development of the dimensional heat release rates of PW configurations during quenching. All cases shown were for a feed pressure of 10 atm. For a short while before quenching, a two-peak behaviour of the total heat release was observed for the stoichiometric (Figs. 9a–d) and lean (Fig. 9e) cases, although not clearly in the rich case (Fig. 9f). To make the development visible in the graphs, the vertical axes were chosen such that the peaks exceeded the graphs. Therefore, the value of the peak was written into each graph. The maximum value of the overall heat release rate (which defined the quenching instance) was found at the wall ($x = 0$) in all cases.

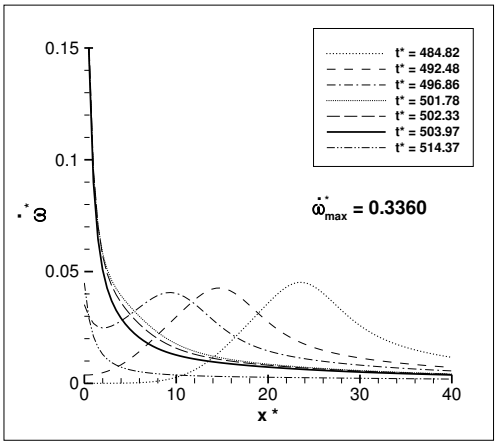

(a) PW, total HR, $\phi_u = 1.0$

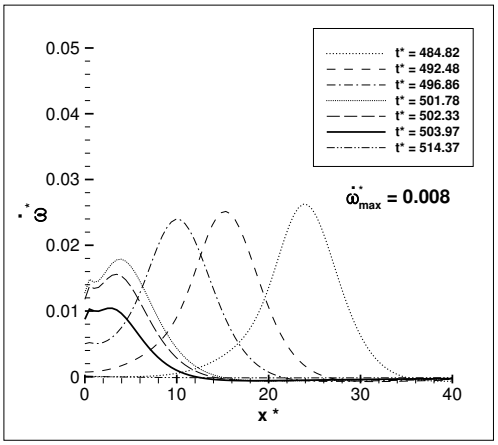

(b) PW, HR of R3f, $\phi_u = 1.0$

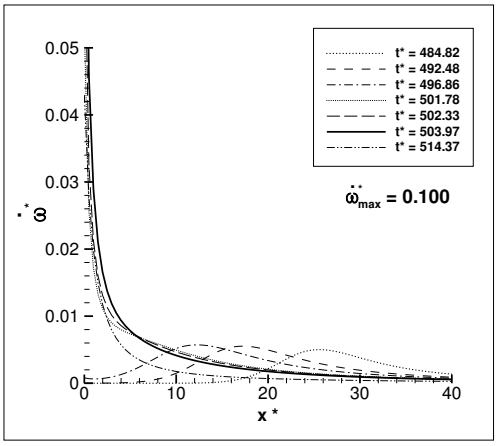

(c) PW, HR of R5r, $\phi_u = 1.0$.

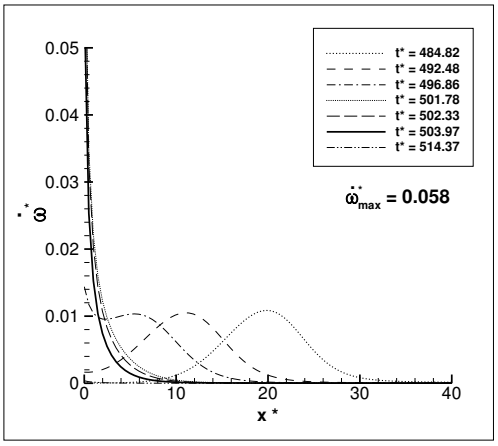

(d) PW, HR of R9f, $\phi_u = 1.0$

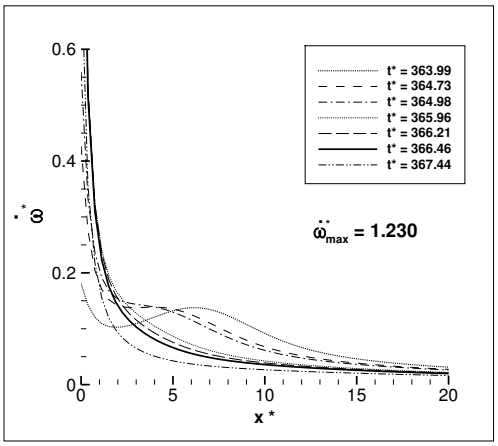

(e) PW, total HR, $\phi_u = 0.5$.

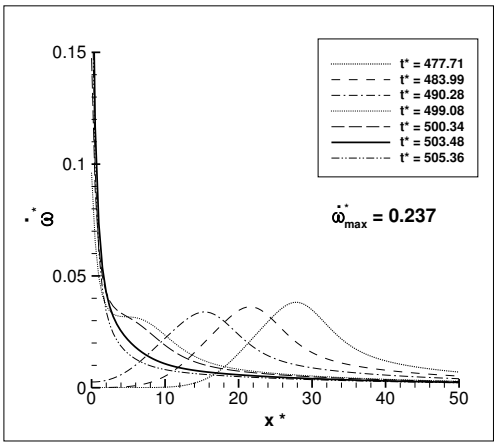

(f) PW, total HR, $\phi_u = 1.5$.

Fig. 9: Non-dimensional heat release rates (HR), $\dot{\omega}^*$, of PW configuration, overall (total) HR and of selected individual elementary reactions. The solid lines represent the quenching instanc21

3.4. Dilution with nitrogen and water vapour

In the following section, we investigate the influence of dilution by N_2 and H_2O of the stoichiometric premixed flame for both impermeable and permeable wall configuration. The PW cases were conducted at $p^{\mathrm{f}}_{\mathrm{H_2}} = 10\,\mathrm{atm}$.

Table 4 specifies the cases where the stoichiometric hydrogen-air mixture presented above (here denoted as Case D0) was compared to cases where more nitrogen (Cases D1 and D2) or more water vapour (Cases D3 and D4) were added. For all these cases the stoichiometric H_2–O_2 ratio, the unburned and wall temperatures $T_{\mathrm{u}} = T_{\mathrm{w}} = 750\,\mathrm{K}$ and (for PW) the feed pressure $p^{\mathrm{f}}_{\mathrm{H_2}}$ at 10 atm were maintained. Each case was run for both IW and PW.

Table 4: Inert gas and water addition to hydrogen-air mixture with wall maintained at 750 K. Case D0 is the undiluted case described above.

Case	$(N_2/O_2)_u$	$(H_2O/O_2)_u$	$(H_2O/H_2)_u$	S^0_{L}	q^0_l	T_{b}	$(\delta_{\mathrm{L}}/S^0_{\mathrm{L}})$
	[-]	[-]	[-]	[m/s]	[MW/m^2]	[K]	[10^{-6} s]
D0	3.762	0.0	0.0	10.8	10.05	2597.5	1.83
D1	4.0	0.0	0.0	10.4	9.20	2511.5	11.6
D2	4.762	0.0	0.0	9.05	7.43	2383.8	60.4
D3	3.762	0.238	0.12	10.4	9.24	2499.8	10.2
D4	3.762	0.5	3.417	8.75	7.36	2343.8	73.0

The resulting non-dimensional wall heat fluxes are shown in Fig. 10. When viewing these quantities, it is worth noting that the flame properties, Table 4, also changed. For both wall configurations, the (dimensional) wall heat fluxes decreased for increasing N_2 dilution due to the lower total reaction heat release rate, $\dot{\omega}$. Reduction by 30% and 54.2% in $\dot{\omega}$ were observed for Cases D1 and D2, respectively, in comparison to Case D0. When adding H_2O, the heat release rate was reduced by 8% and 57%, respectively, for Cases D3 and D4 compared to Case D0. In these simulations, any reaction with N_2 was neglected, while H_2O participated in the reactions according to the chemical mechanism. Dilution with N_2 and H_2O delayed the flame quenching.

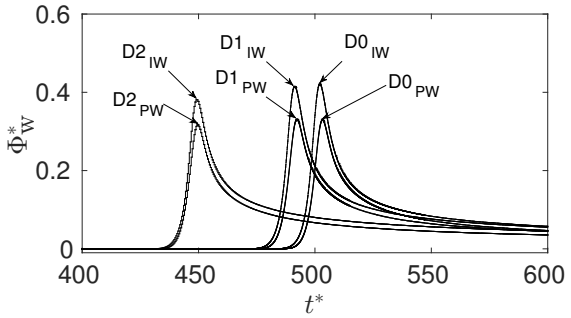

(a) N_2 (inert) dilution

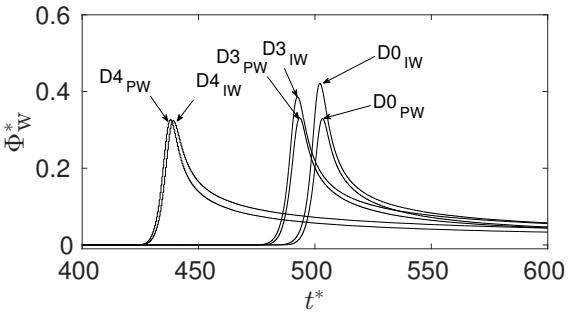

(b) H_2O dilution

Fig. 10: Transient wall heat fluxes for varying dilution by N_2 and H_2O in IW and PW configurations. Here $p^{\mathrm{f}}_{\mathrm{H_2}}$ is maintained at 10 atm for PW, and $T_{\mathrm{w}} = T_{\mathrm{u}} = 750\,\mathrm{K}$.

3.5. Effects of varying wall and unburnt mixture temperature

Simulations with reduced wall and unburnt mixture temperature are presented in this section. The isothermal boundary condition $T_{\mathrm{w}} = T_{\mathrm{u}}$ (Eq. 7) was maintained. Cases with temperatures of 300 K and 500 K, and equivalence ratios of 0.5, 1.0 and 1.5, were computed for comparison with the 750 K cases studied in Sect. 3.2. Here, $p^{\mathrm{f}}_{\mathrm{H_2}}$ was 10 atm for PW.

Non-dimensional values of wall heat and mass fluxes are shown in Fig. 11 for the IW and PW configurations at stoichiometric conditions. The quenching wall heat fluxes decreased with decreasing temperature at the wall. As for dilution, Sect. 3.4, it is worth noting the stronger reduction of the dimensional quantities compared to the non-dimensional. For PW at the lower temperature (300 K), the quenching wall heat flux was marginally higher

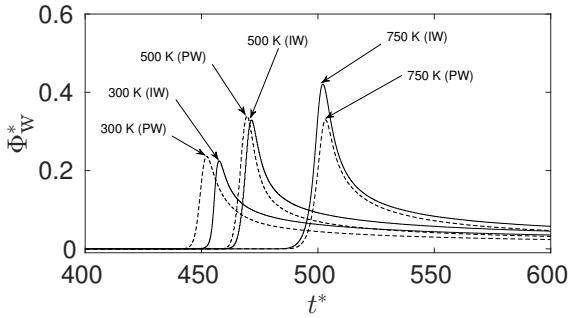

(a) Transient wall heat flux

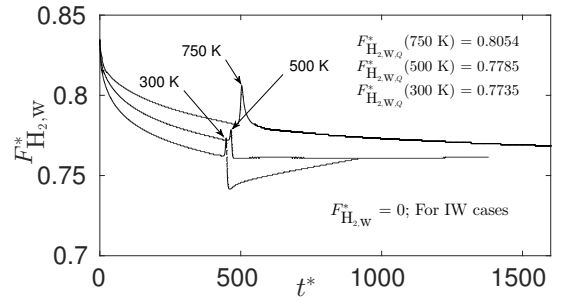

(b) Transient wall H_2 mass flux

Fig. 11: Variation of wall and unburnt temperature ($T_w = T_u$) at stoichiometric conditions for IW and PW. Here, $p^f_{H_2} = 10\,atm$ for PW. The arrows point at the peak values.

(0.05%) compared to IW, whereas at the higher temperatures it was lower than for IW.

Results for rich and lean mixtures are shown in Fig. 12. As seen above for 750 K, the quenching wall heat fluxes of lean PW cases were significantly higher than for IW and lower for a rich mixture. In all cases, the quenching was delayed, and the wall heat flux reduced, with lower temperature.

4. Discussion

4.1. Thermal radiation

Following previous work [5, 7, 8], thermal radiation was neglected as it was not implemented in the code used. This was based on an assumption that the influence was small and negligible due to the optically thin hydrogen

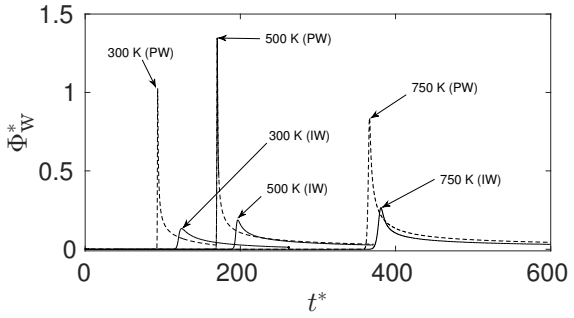

(a) Lean, $\phi_u = 0.5$

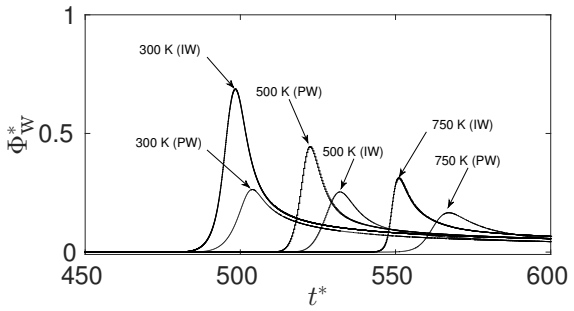

(b) Rich, $\phi_u = 1.5$

Fig. 12: Transient wall heat fluxes for lean and rich mixures at different wall temperatures.

flame.

As a simplified evaluation of the assumption, we did a postprocessing calculation to estimate the radiation emission, using the "optically thin flame model" [38, 39]. The emitted radiation at the highest temperature was 6 orders of magnitude less than the reaction heat release. That is, for the undisturbed propagating flame. Close to the wall, the reaction heat release increased by more than one order of magnitude. For the time instances at quenching and one FWI time (cf. Fig. 8) before quenching, the reaction heat release within the flame was 5-7 orders of magnitude larger than the radiation emission. We also estimated the radiation heat transfer from the flame to the wall and found that it was 5 to 8 orders of magnitude less than the evaluated heat transfer to the wall (conduction, convection). Furthermore, at an emissivity approximately 0.1, the radiation from the wall would balance

the radiation to the wall.

Accordingly, it could be concluded that neglecting radiation heat transfer was justified for this configuration.

4.2. Stages of head-on quenching

Results for the impermeable wall (IW) can be compared to earlier flame-wall interaction (FWI) studies performed for comparable conditions of hydrogen flames [5, 7, 14]. The main quantitative deviations can be explained by the difference between air and oxygen used as oxidizer. Some lesser differences can be attributed to differences in models (chemical mechanism, transport and thermodynamic properties) and numerical methods.

Following [5], head-on quenching can be described as a sequence of three stages to explain FWI characteristics, as indicated in Fig. 2. The first stage is the freely propagating flame under no influence of wall effects such as wall heat flux and (for PW) wall mass flux of fuel. The transient heat release occurred within the travelling reaction zone, and the major heat release reactions were (in decreasing order) R3f, R8f, R9f, R11f and R7f, together with one major endothermic reaction, R1f.

Stage II of the IW case started at $t^* = 494.0$ with corresponding $\mathrm{Pe} \approx \mathrm{Pe_F} = 10.9$. Shortly after, the heat release rate $\dot{\omega}^*$ began increasing and its peak reached the wall ($\mathrm{Pe} = 0$), Fig. 3. The heat release peak reaching the wall is regarded [5] a characteristic of a "hot wall". This instance was at $t^*_\mathrm{Q} - t^* = 5.3$, which, independent of the initial time, can be compared to the values 6 of [5] and 3.4 of [7], both for H_2–O_2 flames. The IW results here were in agreement with the previous studies. Towards quenching, the overall heat release rate increased tenfold due to the radical recombination reactions R8f and R9f and the chain branching R11f at the wall. Said reactions contributed 82% of the overall heat release rate at the wall.

In the PW case, the second stage started earlier than in the IW case. The initial rise of $-\dot{\omega}^*_\mathrm{F}$ was observed at $t^* = 396.0$, with corresponding $\mathrm{Pe} \approx \mathrm{Pe_F} = 116$. Fuel accumulated near the wall while the flame propagated in the first stage. The flame thickness δ^*_L gradually decreased from $t^* = 403.5$, followed by an increase due to the increased ratio of fuel to O_2. Like IW,

the PW flame reached the wall (Pe = 0) before quenching. It was noted that δ_L^* during flame quenching was approximately 1.5 times that of the IW case. Moreover, the wall heat flux was reduced to 78% of the IW case.

Figures 4c and d present transient heat release rates of the PW case. The maximum overall heat release rate during quenching was reduced to 82% of the IW case. This reduction can be explained by the increasingly off-stoichiometric fuel-air mixture. Furthermore, the exothermic Reaction R5r was considerably more important in PW than IW, while consuming H radicals and thereby damping the (more exothermic) H radical consuming Reaction R8f.

In the third stage the heat release and fuel consumption rates of both wall configurations decreased slowly to zero with incomplete combustion. For IW, the widening reaction zone (increasing Pe_F) after flame quenching indicated that remaining H_2 diffused towards the pool of O and OH radicals in the hot burned gas mixture to achieve post-flame oxidization. For PW, the maintained fuel influx gave rapid transport of H_2 towards the hot burned gas.

All three stages remained similar over varying permeate feed pressure of the PW and varying equivalence ratio.

Figure 6b presents the transient non-dimensional wall mass flux ($F^*_{H_2,w}$) at stoichiometric conditions. It was observed that initially, the fuel mass flux decreased in the free propagation state. This can be explained from the accumulation of H_2, reducing the driving force. As the flame approached the wall, from $t^* = 419$, the accumulated fuel was consumed gradually through R5f (H_2 dissociation into H) and decreasing the permeate-side partial pressure of H_2. At quenching, the wall mass flux reached its maximum value.

Figure 5 displays transient profiles of all species mass fractions at the wall ($x = 0$) for both IW and PW. For Stage I of IW, the composition was unaltered because the wall temperature of 750 K was insufficient to promote chain-branching reactions. The onset of changes occurred at $t^* = 494.0$ as the near-wall mixture came under influence of the flame, and the preheat zone of the flame began to loose heat to the colder wall. H_2 and O_2 were consumed at the wall in Reactions R1f, R2f, R3f and R9f with gradual accumulation of

radicals. The intermediate species H_2O_2 was produced through R15r. After quenching, radicals were consumed due to recombination reactions with zero activation energy; R8f and R9f, with influence of R11f (low activation energy, chain branching).

HO_2 accumulated at the wall earlier than other species because of the radical recombination Reaction R9f (zero activation energy), which occurred in the lower-temperature region near the wall in front of the flame. It gradually reached a peak mass fraction value of $3.0 \cdot 10^{-4}$ at $t^* = 490.7$. Just after quenching, the H_2O_2 peak mass fraction value of $3.12 \cdot 10^{-5}$ was observed at $t^* \approx 502.7$ due to the HO_2 consuming Reaction R14f. The H_2O_2 profile showed a behaviour similar to that of the overall heat release, cf. [5]. The H_2O formation at the wall is due to R8f, R16f and R13f involving H and OH radicals. After $t^* = 518$, all species except H_2O declined towards zero because leftover radicals diffused from the colder wall to the hot burned gas region with production of H_2O.

In the PW case, the H_2 and O_2 mass fractions gradually changed by permeation from the beginning. As the mixture at the wall came under influence of the propagating flame, accumulated H_2 dissociated in Reaction R5f to H radicals. The HO_2 accumulation showed similarity to IW and gradually reached an early peak value of mass fraction $3.60 \cdot 10^{-4}$ at $t^* = 493.0$, while H_2O_2 reached its peak value of $1.08 \cdot 10^{-5}$ just before quenching ($t^* = 501.6$). Different from IW, these intermediates and O_2 decreased much faster for PW as permeation of hydrogen interferes with excess production of H and consumption of other radicals near the wall during flame quenching. The consumption of radicals H and OH resulting to zero was more rapid than for IW due to Reactions R2f, R4f, R12f for H and R3f for OH radicals. Furthermore, the behaviour of H_2O_2 was not similar to the overall heat release. The peak of HO_2 for PW was higher than IW due to consumption of H_2O_2 through radical recombination reactions, R17f and R18f. A peak mass fraction value of 0.271 for H_2O was observed at $t^* = 518.0$ due to R3f with consumption of OH radicals at the wall. After $t^* = 518.0$, H_2O was observed to be reduced due to absence of OH radicals at the wall.

At the wall, HO_2 was to a large extent produced through reaction R9f

(as observed by [5] for IW), which is exothermic and have zero activation energy. This was also the case for PW. H_2O_2 was consumed by R15f and R19f until the flame reached the wall for IW. For PW, R15f remained the main consumer, while R19f was of low importance close to the wall.

4.3. Influence of varying feed pressure ($p^{\mathrm{f}}_{H_2}$) and equivalence ratio (ϕ_{u}) on wall heat flux

The primary effect of fuel permeation through the wall (membrane) is to increase the local fuel-to-oxidizer ratio (local equivalence ratio) on the permeate side. The increasing feed pressure increases the fuel wall flux. Indeed, the associated increase in the permeate fuel partial pressure, will tend to reduce the mass flux according to Eq. 5. However, as seen in Fig. 7a (and more so from the corresponding graph of the dimensional quantity, not shown), this was a minor effect. The realization of the increased local equivalence ratio showed a modest dependency on that of the initial, undisturbed mixture. All the PW cases gave a locally very rich mixture close to the wall (as seen in graph f of Figs. 4-6 of [17]). This can explain why the maximum wall heat flux of the PW cases had a weak sensitivity to the the initial equivalence ratio (ϕ_{u}) compared to IW. Moreover, at a location not far from the wall, the mixture approached stoichiometric conditions. Hence, the fuel conversion rates were still large close to the wall.

The very rich IW case ($\phi_{\mathrm{u}} = 4.0$) behaved in many aspects similar to the lean PW case ($\phi_{\mathrm{u}} = 0.5$, 10 atm feed pressure). The (dimensional) wall heat flux at quenching for these two cases were close to each other. Also the reactions of importance for heat release were also the same, except that Reactions R5f and R9f changed place as the 2nd and 3rd most important (after R8f).

4.4. Heat release rate trend on varying equivalence ratio (ϕ_{u}) in PW configurations

In both the stoichiometric (Fig. 9a) and fuel-lean (Fig. 9e) cases, a two-peak behaviour of the total heat release rate was observed near the wall. The main contributor to the peak moving towards the wall appeared to be

Reaction R3f (Fig. 9b), and to some extent R9f (Fig. 9d). The peak at the wall was made by Reactions R8f, R5r (Fig. 9c), R9f and R11f until the peaks merged. On the other hand, the fuel-rich case (Fig. 9f) barely had a two-peak behavior, as the moving peak reached the wall in about the same instance as the wall-peak was rising. For none of the cases, the described behaviour led to any two-peak temperature profile.

4.5. Influence of dilution

Increased dilution reduced the temperature of the burnt gases and, consequently, reduced the wall heat fluxes (Fig. 10). The thermal gradient alone influenced the wall heat fluxes. Additional N_2 (inert) did not influence major heat releasing reactions, however, it did reduce the total reaction heat release rate due to its increased mole fraction. Similarly, a non-diluted H_2–O_2 premixed flame gave higher wall heat fluxes [7].

Close to the wall near quenching, dilution did not alter the relative importance of reactions. However, in the freely propagating flame, H_2O dilution caused reaction R8f to become more important for heat release than R3f.

4.6. Effects of changing wall temperature on wall heat flux

For both IW and PW configurations, the quenching wall heat fluxes (Figs. 11 and 12) increased approximately linearly with increasing wall temperature. In Fig. 11b is seen that at 300 K, after quenching, the PW wall H_2 flux dropped after quenching and then, gradually increased. This increase was caused by diffusion of H_2 away from the wall and hence, increased the pressure difference over the permeable wall (cf. Eq. 5). Apparently, this effect has lesser impact at higher temperatures.

The radical recombination reactions R8f and R9f played the most important roles for heat release rate at the wall for all cases. Next to these, Reactions R11f and R13f were important for IW at 750 K. At lower temperatures, R11f became much less important. For PW at 750 K, Reactions R5r and R11f were the important reactions next to R8f and R9f. At 300 K, R5r had lost its role and R13f became more important than R11f in the near-wall heat release.

The accumulation of intermediate species (HO_2 and H_2O_2) was higher for both IW and PW at lower temperatures as compared to 750 K.

5. Conclusions

The interactions of a 1-D head-on flame with an impermeable wall (IW) and a permeable wall (PW) was investigated for premixed hydrogen–air mixtures. Additional fuel was released through the permeable wall.
For rich and stoichiometric mixtures, PW with fuel influx gives a moderate reduction of the quenching (i.e. maximum) wall heat flux compared to IW (22% reduction was seen for stoichiometric), whereas for a lean mixture, there was a considerable increase. The maximum reaction heat release rate occurred at the wall in all cases studied. Influence of the wall on flame is felt much earlier, that is, more distant from the wall, for PW than for IW.
Permeation of fuel through the wall gives a locally richer flame at the wall for PW. With a detailed chemical mechanism (Li et al. [22]) it can be seen more H radicals and less O radicals are present close to the wall for PW. The exothermic reaction recombining 2H to H_2 is considerably more important for PW. This consumption of H inhibit the more exothermic reaction of OH and H to H_2O.
Both a lower initial temperature and dilution with N_2 (inert) or H_2O (participating) reduce the burned-mixture temperature and, consequently, the wall heat flux. Also the flame propagation and quenching is delayed.

Acknowledgements

The work of the 1st author (Salimath) was partly funded by the Research Council of Norway through the project CCERT-CO2 Capture with Enabling Research and Technology, while the work at SINTEF (Gruber) has been conducted with support from the BIGCCS Centre, performed under the Norwegian research program Centres for Environmental Friendly Energy Research (FME). The authors acknowledge the following partners for their contributions: ConocoPhillips, Gassco, Shell, Statoil, Total, GDF Suez and

the Research Council of Norway (193816/S60). We are grateful to the Norwegian Metacenter for Computational Science (NOTUR) for providing the HPC computational resources and useful technical support.

AppendixA. Comparison with Chemkin calculations

The flame properties above were obtained from a freely propagating flame by S3D [19]. Since the Chemkin code is widely used to produce such properties, a comparison was made by using the Chemkin library [31, 32]. The chemical mechanism and specific heats were identical. For the variation of ϕ_{u} from 0.5 to 1.5, the Chemkin results gave a 4-2% lower $(T_{\mathrm{b}} - T_{\mathrm{u}})$, a 9-5% higher S_{L}^0 and a 7-4% lower δ_{L} compared to S3D. There are some differences in the algorithms and numerical setups used in these two options, which can explain the deviations.

Figure A.13 shows the mass-fraction profiles for the stoichiometric flame for both codes. The abscissa x' is the distance from the point of the maximum temperature gradient, non-dimensionalized by the thermal flame thickness δ_{L}^0. The S3D results were taken at a the instance of 0.65 times the quenching time.

Nomenclature

Abbreviations

IW	Impermeable wall
PW	Permeable wall

Greek symbols

δ_{L}^0	Flame thickness	m
δ_{L}	Characteristic flame thickness	m
$\dot{\omega}$	Overall reaction heat release rate	$\mathrm{W/m^3}$
$\dot{\omega}_k$	Molar production rate of species k	$\mathrm{kg/(m^3 s)}$
λ	Thermal conductivity of the gaseous mixture	W/(mK)
Φ	Heat flux	$\mathrm{W/m^2}$
ϕ	Equivalence ratio	$-$
ρ	Density	$\mathrm{kg/m^3}$

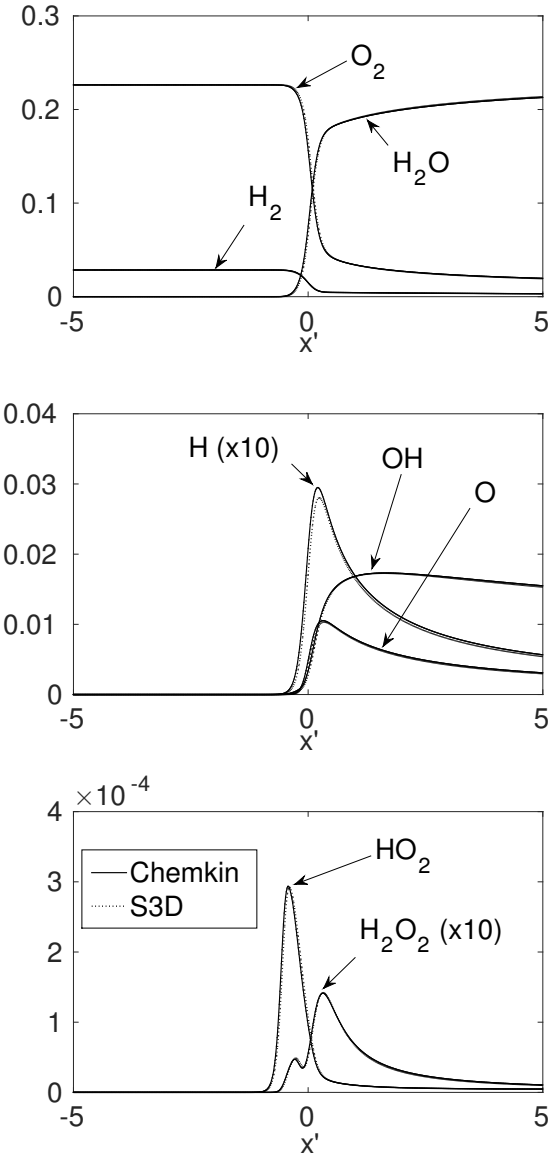

Fig. A.13: Species mass fractions of the freely propagating flame. Comparison of results of the Chemkin library and of S3D.

τ	Viscous stress tensor	$\mathrm{N/m^2}$
Latin symbols		
Pe	Peclet number based on location of $\dot{\omega}_{\max}$	$-$
$\mathrm{Pe_F}$	Peclet number based on location of $-\dot{\omega}_{\mathrm{F,max}}$	$-$
C_p	Specific heat at constant pressure	J/(kgK)
D	Mass diffusivity	$\mathrm{m^2/s}$
e_0	Specific total energy	$\mathrm{J\,kg^{-1}}$
F_k	Mass flux of species k	$\mathrm{kg/(m^2 s)}$
L	Length of domain	m
m	Parameter (exponent) for heat flux estimation	$-$
n	Pressure exponent of membrane	$-$
N_g	Number of species	$-$
N_r	Number of reactions	$-$
p	Pressure	Pa
q_l^0	Flame power	$\mathrm{W/m^2}$
S_L^0	Laminar flame speed	$\mathrm{m\,s^{-1}}$
T	Temperature	K
t	Time	s
u	Velocity	$\mathrm{m\,s^{-1}}$
V_k	Mass diffusion velocity of species k	$\mathrm{m\,s^{-1}}$
W_k	Molecular weight of species k	kg/kmol
x	Spatial coordinate	m
X_k	Mole fraction of species k	$-$
y	Wall-flame distance	m
Y_k	Mass fraction of species k	$-$
Superscripts		
0	Free propagating state	
f	Feed side	
p	Permeate side	
Subscripts		
$'$	Non-dimensional values	
$*$	Non-dimensional values	
α,β	Directional indices	

b	Burnt mixture
FWI	Flame wall interaction
F	Fuel
max	Maximum value
mix	Mixture average
Q	Quenching
u	Unburnt mixture
w	Wall
k	Species index

References

[1] C. K. Westbrook, A. A. Adamczyk, G. A. Lavoie, A numerical study of laminar flame wall quenching, Combust. Flame 40 (1981) 81–99.

[2] I. S. Wichman, G. Bruneaux, Head-on quenching of a premixed flame by a cold wall, Combust. Flame 103 (4) (1995) 296–310.

[3] A. Gruber, R. Sankaran, E. R. Hawkes, J. H. Chen, Turbulent flame wall interaction: a direct numerical simulation study, J. Fluid Mech. 658 (2010) 5–32.

[4] O. A. Ezekoye, R. Greif, R. F. Sawyer, Increased surface temperature effects on wall heat transfer during unsteady flame quenching, Symp. Combust. 24 (1) (1992) 1465–1472.

[5] F. Dabireau, B. Cuenot, O. Vermorel, T. J. Poinsot, Interaction of flames of H2 + O2 with inert walls, Combust. Flame 135 (1-2) (2003) 123–133.

[6] P. Popp, M. Baum, Analysis of wall heat fluxes, reaction mechanisms, and unburnt hydrocarbons during the head-on quenching of a laminar methane flame, Combust. Flame 108 (3) (1997) 327–348.

[7] R. Owston, V. Magi, J. Abraham, Interactions of hydrogen flames with walls: Influence of wall temperature, pressure, equivalence ratio, and diluents, Int. J. Hydrogen Energy 32 (12) (2007) 2094–2104.

[8] R. Mari, B. Cuenot, J.-P. Rocchi, L. Selle, F. Duchaine, Effect of pressure on hydrogen/oxygen coupled flame wall interaction, Combust. Flame 168 (2016) 409–419.

[9] B. Boust, J. Sotton, S. A. Labuda, M. Bellenoue, A thermal formulation for single-wall quenching of transient laminar flames, Combust. Flame 149 (3) (2007) 286–294.

[10] A. Dreizler, B. Böhm, Advanced laser diagnostics for an improved understanding of premixed flame-wall interactions, Proc. Combust. Inst. 35 (1) (2015) 37–64.

[11] J. H. Lu, O. A. Ezekoye, R. Greif, R. F. Sawyer, Unsteady heat transfer during side wall quenching of a laminar flame, Symp. Combust. 23 (1) (1991) 441–446.

[12] S. Vosen, R. Greif, C. Westbrook, Unsteady heat transfer during laminar flame quenching, Symp. Combust. 20 (1) (1985) 75–83.

[13] J. Sotton, B. Boust, S. A. Labuda, M. Bellenoue, Head-on Quenching of Transient Laminar Flame: Heat Flux and Quenching Distance Measurements, Combust. Sci. Technol. 177 (7) (2005) 1305–1322.

[14] T. Poinsot, D. Veynante, Theoretical and Numerical Combustion, R.T. Edwards, Inc., 2005.

[15] W. M. Huang, S. R. Vosen, R. Greif, Heat transfer during laminar flame quenching: Effect of fuels, Symp. Combust. 21 (1) (1988) 1853–1860.

[16] A. Gruber, J. H. Chen, D. Valiev, C. K. Law, Direct numerical simulation of premixed flame boundary layer flashback in turbulent channel flow, J. Fluid Mech. 709 (2012) 516–542.

[17] A. Gruber, P. S. Salimath, J. H. Chen, Direct numerical simulation of laminar flame-wall interaction for a novel H2-selective membrane/injector configuration, Int. J. Hydrogen Energy 39 (11) (2014) 5906–5918.

[18] K. Jordal, R. Anantharaman, A. Gruber, T. Peters, P. P. Henriksen, D. Berstad, R. Bredesen, Performance of the IGCC with distributed feeding of H2 in the gas turbine burner, Energy Procedia 63 (2014) 2037–2044.

[19] J. H. Chen, A. Choudhary, B. de Supinski, M. DeVries, E. R. Hawkes, S. Klasky, W. Liao, K. Ma, J. Mellor-Crummey, N. Podhorszki, R. Sankaran, S. Shende, C. S. Yoo, Terascale direct numerical simulations of turbulent combustion using S3D, Comput. Sci. Discov. 2 (1) (2009) 15001.

[20] R. Bredesen, K. Jordal, O. Bolland, High-temperature membranes in power generation with CO2 capture, Chem. Eng. Process. Process Intensif. 43 (9) (2004) 1129–1158.

[21] M. Vadrucci, F. Borgognoni, A. Moriani, A. Santucci, S. Tosti, Hydrogen permeation through Pd-Ag membranes: Surface effects and Sieverts' law, Int. J. Hydrogen Energy 38 (10) (2013) 4144–4152.

[22] J. Li, Z. Zhao, A. Kazakov, F. L. Dryer, An updated comprehensive kinetic model of hydrogen combustion, Int. J. Chem. Kinet. 36 (10) (2004) 566–575.

[23] J. H. Chen, Petascale direct numerical simulation of turbulent combustion - Fundamental insights towards predictive models, Proc. Combust. Inst. 33 (1) (2011) 99–123.

[24] R. Sankaran, E. R. Hawkes, J. H. Chen, T. F. Lu, C. K. Law, Direct numerical simulations of turbulent lean premixed combustion, J. Phys. Conf. Series 46 (1) (2006) 38–42.

[25] R. W. Grout, A. Gruber, C. S. Yoo, J. H. Chen, Direct numerical simulation of flame stabilization downstream of a transverse fuel jet in crossflow, Proc. Combust. Inst. 33 (1) (2011) 1629–1637.

[26] E. R. Hawkes, R. Sankaran, J. C. Sutherland, J. H. Chen, Scalar Mixing in DNS of Temporally-Evolving Plane Jet Flames with Detailed CO/H2 Kinetics, Proc. Combust. Inst. 31 (1) (2007) 1633–1640.

[27] D. O. Lignell, J. H. Chen, P. J. Smith, T. Lu, C. K. Law, The effect of flame structure on soot formation and transport in turbulent nonpremixed flames using direct numerical simulation, Combust. Flame 151 (1-2) (2007) 2–28.

[28] R. Sankaran, H. G. Im, E. R. Hawkes, J. H. Chen, The effects of non-uniform temperature distribution on the ignition of a lean homogeneous hydrogen-air mixture, Proc. Combust. Inst. 30 (1) (2005) 875–882.

[29] T . Echekki, J. H. Chen, Direct numerical simulation of auto-ignition in non-homogenous hydrogen-air mixtures, Combust. Flame 134 (3) (2003) 169–191.

[30] C. A. Kennedy, M. H. Carpenter, Several new numerical methods for compressible shear layer simulations, Appl. Numer. Math. 14 (804) (1994) 397.

[31] R. J. Kee, F. M. Rupley, J. A. Miller, CHEMKIN-II: A FORTRAN chemical kinetics package for the analysis of gas phase chemical kinetics, SANDIA Rep. No. SAND89-8009B (1989) 3–164.

[32] R. J. Kee, L. G. Dixon, J. Warnatz, M. E. Coltrin, J. A. Miller, H. K. Moffat, A fortran chemical kinetics package for the analysis of gas-phase chemical kinetics., Tech. Rep., Release 3.5, Reaction Design Inc., San Diego, CA, 1999.

[33] B. Gustafsson, A. Sundström, Incompletely Parabolic Problems in Fluid Dynamics, SIAM J. Appl. Math. 35 (2) (1978) 343–357.

[34] J. Nordström, M. Svärd, Well-Posed Boundary Conditions for the Navier–Stokes Equations, SIAM J. Numer. Anal. 43 (3) (2005) 1231–1255.

[35] J. C. Strikwerda, Initial boundary value problems for incompletely parabolic systems, Commun. Pure Appl. Math. 30 (6) (1977) 797–822.

[36] C. Yoo, Y. Wang, A. Trouve, H. Im, Characteristic Boundary Conditions for Direct Simulations of Reacting Counterflow, Combust. Theory Model. 9 (1) (2005) 617–646.

[37] C. S. Yoo, H. G. Im, Characteristic boundary conditions for simulations of compressible reacting flows with multi-dimensional, viscous and reaction effects, Combust. Theory Model. 11 (2) (2007) 259–286.

[38] Radiation Models, URL `http://www.sandia.gov/TNF/radiation.html`, (accessed: 2017-11-25), 2003.

[39] R. Barlow, N. S. A. Smith, J.-Y. Chen, R. W. Bilger, Nitric oxide formation in dilute hydrogen jet flames: isolation of the effects of radiation and turbulence-chemistry submodels, Combust. Flame 117 (1999) 4–31.